RESEARCH ARTICLE

Low-Cost and Compact Disposable Extracorporeal Centrifugal Blood Pump Utilizing a Homopolar Bearingless Switched Reluctance Slice Motor

REN YANG [ID]**1, ZEQIANG HE**1, **NAOHIRO SUGITA** [ID]**2,**
AND TADAHIKO SHINSHI [ID]**2, (Member, IEEE)**

1Department of Mechanical Engineering, Tokyo Institute of Technology, Yokohama 226-0026, Japan
2Institute of Innovative Research, Tokyo Institute of Technology, Yokohama 226-0026, Japan

Corresponding author: Tadahiko Shinshi (shinshi.t.ab@m.titech.ac.jp)

ABSTRACT The high biocompatibility and high durability of disposable extracorporeal centrifugal blood pumps (CBPs) utilizing magnetic bearing or bearingless motor technology make them perfect for supporting cardiopulmonary circulation for patients. However, the rotor incorporated in the disposable unit typically uses high-cost and environmentally-unfriendly rare-earth permanent magnets (PMs), leading to economic and environmental issues. This paper proposes a centrifugal blood pump with a PM-free impeller/rotor in the disposable pump head utilizing a 12/8 bearingless switched reluctance slice motor (BELSRM). Two axial-magnetized PM rings and two iron rings are mounted symmetrically above and below the tips of the stator poles. The biased magnetic flux generated by the PM rings forms a closed vertical magnetic circuit (homopolar flux circuit) with a PM-free rotor, providing high passive stiffness and large positioning forces independent of the rotor angle. A three-dimensional (3D) finite element analysis (FEA) model was used to evaluate the rotor support stiffness, the current-force coefficient, and the rotational torque. A prototype bearingless slice motor (BELSM) and a disposable pump head with a diameter of 50 mm PM-free impeller/rotor were fabricated. The radial magnetic levitation and the rotation were actively controlled by displacement and speed feedback control systems, respectively. A mock circulatory loop filled with 40wt% aqueous glycerol solution was set to evaluate the performance of the proposed CBP. The CBP provided a maximum flow rate of 4.59 L/min and a maximum head pressure of 214.5 mmHg at 2300 rpm and 2400 rpm, respectively.

INDEX TERMS Bearingless switched reluctance slice motor, disposable pump head, extracorporeal centrifugal blood pump, PM-free rotor.

I. INTRODUCTION

Extracorporeal centrifugal blood pumps (CBPs) placed outside the human body are used to generate a continuous flow and pressure in mechanical circulatory support systems, such as ventricular assist devices (VADs), and extracorporeal membrane oxygenation (ECMO) [1], [2], [3]. Extracorporeal CBPs are either applied for short-term emergency resuscitation or mid-term life extension, such as Bridge to Decision and Bridge to Transplantation, requiring the CBPs to possess

The associate editor coordinating the review of this manuscript and approving it for publication was Ton Duc Do [ID].

high durability and biocompatibility [4], [5], [6]. Commercial rotary blood pumps [7], [8], [9] with blood-immersed mechanical contact bearings are prone to device malfunction and blood thrombosis around the contact area because of material wear and heat generation, making them unsuitable for continuous operation.

To further enhance durability and reduce blood damage, disposable extracorporeal type CBPs have been developed utilizing magnetic bearing or bearingless motor technology to achieve contactless operation and reduce the stagnation flow [10], [11], [12], [13]. Each disposable CBP consists of a reusable electrical-drive unit and a disposable pump

head. The disposable pump head consisting of an integrated impeller/rotor, top housing, and bottom housing is attached and removed just once from the reusable electric drive unit. However, the conventional integrated impeller/rotor in a disposable pump head contains expensive rare-earth magnets in order to realize the magnetic coupling required to generate the motor torque or magnetic levitation, leading to a high cost for the disposal [14], [15].

A CBP with a permanent magnet-free (PM-free) impeller/rotor was proposed to overcome the cost problem. A pure iron rotor with a salient structure on the inner side and a nonsalient structure on the outer side, forms a reusable magnetic coupling torque transmission mechanism and a radial-motion-control magnetic bearing, respectively [16]. However, the complex mechanics of levitation and rotation affects the flexibility of the pump head design and limits the durability of the reusable parts due to the service life of the bearing supporting the motor shaft.

Several bearingless slice motors (BELSM) with PM-free rotors for CBPs with simple mechanisms and high durability have been proposed. These BELSMs remove the internal torque transmission mechanism by forming magnetic fields for levitation and rotation in the same air gap between the rotor and the stator. BELSMs with PM-free rotors can be divided into stator-PM type BELSMs and entirely PM-free type BELSMs depending on the different flux bias generation for magnetic levitation and passive stabilization.

Regarding stator-PM type BELSMs, a heteropolar flux-switching reluctance type bearingless motor was proposed [17], embedding alternative tangentially magnetized PMs in the stator poles. The alternative flux bias generated by the PMs in the air gap provides a flux bias for magnetic levitation and a high torque density for rotation. However, the placement of multiple magnets can lead to a complex structure and significant flux leakage. Furthermore, the negative support stiffness and current-force coefficient in the radial direction are coupled with the rotor rotational angle, leading to complicated suspension control with alternating current (AC). Regarding entirely PM-free type BELSMs, some bearingless slice reluctance motors with a flux bias generated by the winding current were proposed [18], [19]. However, considerable power was consumed to generate the continuous magnetic flux bias required for sufficient passive stiffness, limiting the usage time when running on a battery. Moreover, the additional bias current also leads to severe heat generation.

In this paper we propose a disposable extracorporeal CBP utilizing a novel bearingless switched reluctance slice motor (BELSRM) with a homopolar flux bias generated by PM rings, achieving a more straightforward motor structure, easier radial suspension control, and smaller heat generation. We simulated the electromagnetic field using finite element method (FEM) analysis to design a prototype BELSRM that would provide sufficient average torque and passive stiffness. With this, a prototype extracorporeal CBP was fabricated.
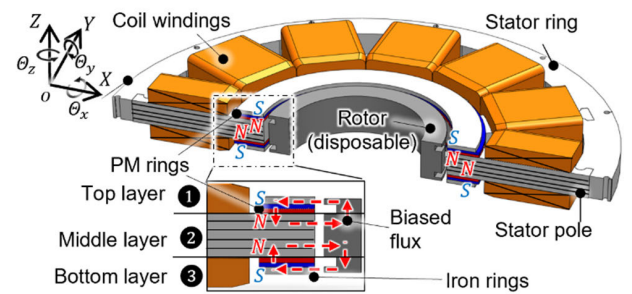

FIGURE 1. Vertical cross-sectional view of the proposed BELSRM.

The BELSRM characteristics and pump performance were experimentally evaluated.

This paper is organized as follows. The basic operating principle of the BELSRM is introduced in Section II, including the structure, the rotor support stiffness, the force generation for radial positioning, and the torque generation for rotation. In Section III, the design target is defined, and the BELSRM characteristics are verified by FEM analysis. The fabrication and assembly of a prototype disposable centrifugal blood pump utilizing a BELSRM together with the electrical hardware and software system is described in Section IV. The magnetic levitation, rotation, and pump performance are evaluated in Section V. Finally, a discussion and the conclusions drawn are contained in Section VI and Section VII.

II. BASIC MECHANISM AND OPERATING PRINCIPLE OF THE PROPOSED BELSRM
A. STRUCTURE
Figs. 1 and 2 show vertical and horizontal cross-sectional views of the proposed BELSRM with a disposable PM-free rotor. The configuration of the BELSRM is similar to a conventional 12/8 switched reluctance motor. The twelve stator poles made of laminated steel are placed symmetrically around the circumference. Each stator pole is wound with a concentrated combined winding to achieve compactness, improve coil manufacturability, and reduce copper loss [20]. The current in each combined winding comprises rotation and suspension currents, which can simultaneously generate rotational torque and a radial suspension force. The outer stator ring is assembled into a single unit with twelve stator poles. The twelve coil windings are divided into four groups X_n, X_p, Y_n, Y_p, and each group has three phases U, V, and W, as shown in Fig. 2. Opposing groups, such as X_n and X_p are used to control the radial position in one direction. The U, V, and W phase windings are used for phase current commutation in the rotational control. The rotor, made of soft iron, is a triple-layer slice structure, as shown in Fig. 1. The top and bottom layers are doubly flanged and are opposite the iron rings. The middle layer has eight rotor teeth opposite the stator poles.

Two vertical-magnetized PM rings are placed symmetrically above and below the tips of the stator poles. Two iron rings are attached to the outside of the PM rings to
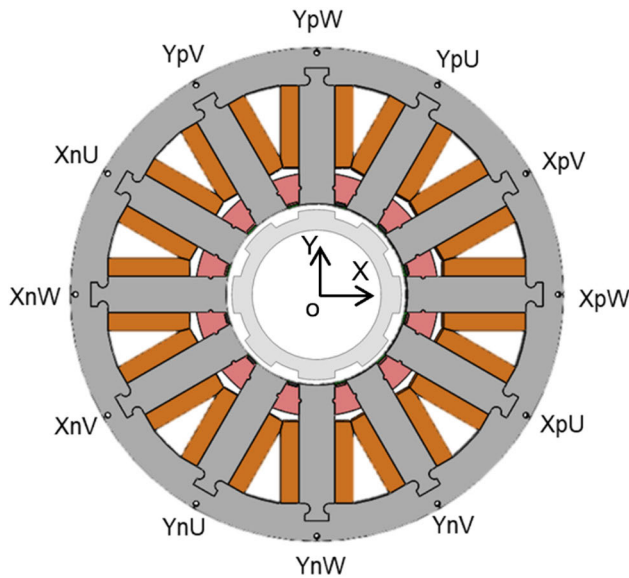
FIGURE 2. Horizontal cross-sectional view of the proposed BELSRM.

FIGURE 3. Principle of passive stiffness by biased flux generated by PM rings.

FIGURE 4. Principle of the force generation for radial positioning.

focus the magnetic flux bias for magnetic levitation, passive stabilization, and rotation. The magnetic flux bias from the PM rings flows through the stator pole, rotor teeth, rotor flange, and the iron rings to form two closed vertical magnetic circuits (homopolar flux circuits). The magnetic flux generated by the phase windings does not penetrate the PM to avoid PM demagnetization, which provides a more dynamic positioning force for radial-motion control.

The BELSRM employs two PM rings and a triple-layer slice structure rotor to constitute a triple-layer slice homopolar magnetic field, as shown in Fig. 1. Two vertical flux biases generated by the PM rings form the magnetic fields in the top and bottom layers. The middle layer's magnetic field is composed of the flux bias generated by the PM rings superimposed on the magnetic flux generated by the windings. The structure of the triple-layer homopolar magnetic field increases the multiple-layer magnetic flux to enhance the passive stiffness for portable applications.

B. PRINCIPLE OF PASSIVE STIFFNESS

Due to the triple-layer slice structure, the rotor is passively stabilized in the axial and tilt directions to simplify the control system and reduce the power consumption, as shown in Fig. 3. Provided that the rotor has axial movement or tilt, the triple-layer homopolar magnetic field will generate restoring reluctance forces and torque to fulfill the principle of least reluctance. Both the restoring reluctance force and torque are proportional to the axial displacement and tilt angle over small deviation ranges, respectively.

C. PRINCIPLE OF FORCE GENERATION FOR RADIAL POSITIONING

Due to the negative stiffness in the radial direction, radial positioning feedback control in the X- and Y-directions is
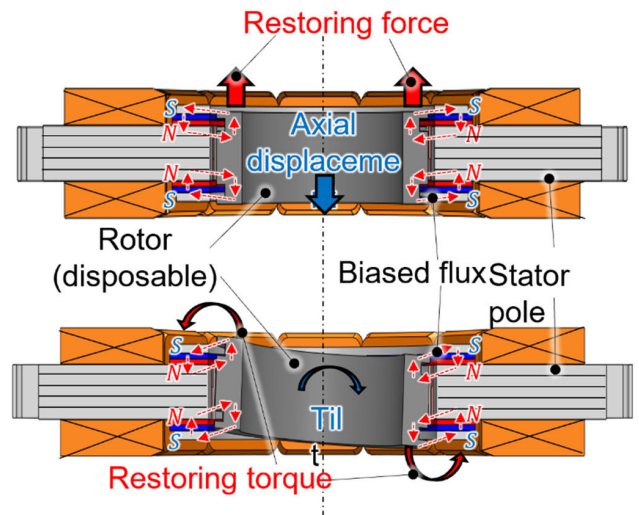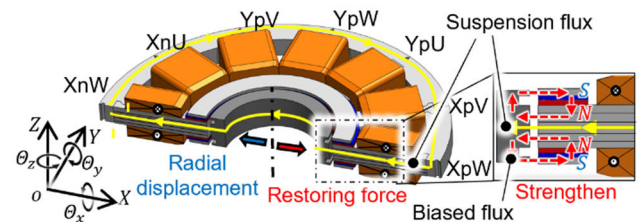
necessary to generate a radial restoring force and avoid contact between the rotor and the stator. Fig. 4 illustrates the principle of radial force generation. The two groups of coil windings X_n and X_p are fed with negative and positive current, respectively, to generate a suspension flux in the X-direction, as shown by the yellow lines in Fig. 4. The magnetic flux density in the air gaps varies due to the superposition of the suspension flux and the flux bias generated by the PM rings. The magnetic flux density in the air gap toward the rotor displacement direction is weakened, and the flux density in the opposite direction is strengthened. A restoring force due to the magnetic flux density difference in the air gap is generated to push the rotor back to equilibrium.

D. PRINCIPLE OF ROTATIONAL TORQUE GENERATION

Fig. 5 shows the principle of rotational torque generation. The magnetic flux in the air gap consists of the flux bias arising from the PM rings and the magnetic flux generated by the coil windings. Therefore, the torque generated by the BELSRM contains not only a reluctance torque but also a permanent magnet torque. The twelve coil windings are divided into four groups, and each group contains U, V, and W phase windings, as shown in Fig. 5. The coil windings with U, V, and W phases are sequentially fed with current. The
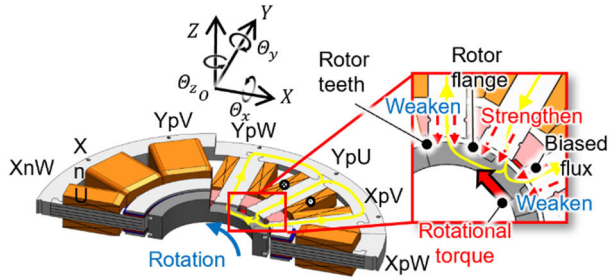
FIGURE 5. Principle of the rotational torque generation.

TABLE 1. Target values and Fem results for the proposed BELSRM.

Parameters	Target values	Simulated results		
		Rotor angle = 0°	Rotor angle = 22.5°	
Negative stiffness K_s (N/mm)	-	-60.4	-56.3	
Current-force coefficient K_c (N/A)	-	19.3	16.1	
Axial stiffness K_z (N/mm)	9.7	18.5	18.0	
Tilt stiffness K_θ (Nm/rad)	2.3	5.9	5.3	
Average torque T_d (Nm)	0.060	0.068		

magnetic flux arising from the energized U phase winding goes from the stator pole into the rotor as does the flux bias, enhancing the magnetic flux density locally in the air gap, as shown in Fig. 5. The magnetic flux passing through the rotor flows out of the V and W stator poles to form two closed circuits, reducing the magnetic density at the corresponding locations. The variation in magnetic flux density in the air gap generates an attractive tangential force to align the rotor teeth with the stator poles of the energized phases. Based on the commutation of three-phase windings, the rotor rotates continuously

III. PROTOTYPE DESIGN

A. DESIGN TARGET

The special performance requirements of the proposed BEL-SRM are magnetic levitation of the PM-free impeller/rotor and sufficient motor torque at a rotational speed that generates an adequate flow rate and head pressure for the centrifugal blood pump. Furthermore, the magnetic levitation mechanism and motors share the same stator core for miniaturization. To simplify the control system, only the radial direction is actively controlled by magnetic levitation. In contrast, magnetic couplings are used for support in the axial direction and to obtain tilt with sufficient passive stiffness. In order for the CBP to have a compact structure the impeller/rotor diameter was chosen to be 50 mm, and the air gap between the rotor and stator was set at 1.5 mm to guarantee a sufficient fluid gap for blood circulation and an adequate chamber wall thickness for mechanical strength, these parameters being determined by previous research [14]. In designing the BELSM, the rotational torque capacity and the passive stiffness are the significant parameters that determine the essential hydraulic performance and the passive stabilization for a given air gap length and volume. A CBP with the above specification is required in order to yield a flow rate above 5 L/min against a head pressure of 250 mmHg (33.3 kPa) for extracorporeal circulation support with an artificial lung [15]. We set the target value of the motor torque and the rotational speed to be the same as in previous research because the impeller profile and dimensions of this prototype are the same as those reported in the references. A rotational torque of more than 0.060 Nm at 3000 rpm is needed to meet the above-mentioned hydraulic requirements. Sufficient passive stiffness of the
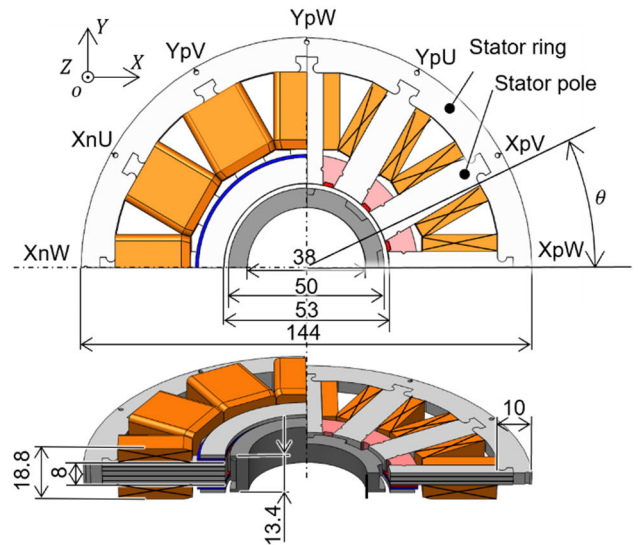

FIGURE 6. 3D simulation model of the proposed BELSRM.

axial and tilt motions is required to avoid contact between the rotor and the chamber wall during levitation and rotation. Previous research [21] suggests that the target passive support stiffnesses in the axial and tilt directions should exceed 9.7 N/mm and 2.3 Nm/rad, respectively, for our rotor design. Table 1 summarizes the target values of the parameters of the proposed BELSRM.

B. NUMERICAL SIMULATION MODEL

The axial and tilt passive stiffnesses K_z and K_θ, the negative radial stiffness K_s, the radial current-force coefficient K_c, and the rotational torque T_d of the proposed BELSRM were obtained by simulation using a three-dimensional (3D) model with FEM software (Ansys, Maxwell 19.0). The total number of mesh elements in the 3D FEA electromagnetic static simulation was 1384492. Fig. 6 illustrates the simulation model when the rotor is positioned at the geometrical center of the BELSRM and the initial rotor angle is the W phase stators aligned with the teeth. Table 2 summarizes the dimensions

TABLE 2. Simulation dimensions of the proposed BELSRM.

Component	Dimension (mm)		Component	Dimension (mm)	
Rotor	Height	13.4	Stator	Outer diameter	144
	Outer diameter	50		Inner diameter	53
	Inner diameter	38		Thickness	8
	Flange thickness	1	PM ring	Thickness	1.8
	Groove depth	2		Inner diameter	53.1
	Teeth thickness	7.8		Outer diameter	71
Iron ring	Thickness	1.3			
	Inner diameter	53			
	Outer diameter	69			

TABLE 3. Simulation material properties and winding configurations of the proposed BELSRM.

Component		Conditions	Component		Conditions
Coil	Total cross-section area (mm^2)	124.8	PM ring	Type	NdFe35
	Turns	386		Coercive force (kA/m)	890
Rotor	Soft iron			Remanence (T)	1.20 T
Stator	Lamination steel		Iron ring		Soft iron

of the 3D model. Some structural parameters were evaluated to generate the required rotational torque by increasing the magnetic flux bias in the air gap and the cross-sectional area of the coil for sufficient magnetomotive force. Firstly, the thickness of the PM rings and the outer diameter of the iron rings were examined to focus on and increase the magnetic flux bias in the air gap. Secondly, the outer diameter of the stator rings was examined to increase the cross-sectional area of the coil. The material properties and winding configurations of the simulation model are shown in Table 3. The angular position θ, where the W phase stator pole is aligned with the rotor teeth, is defined as 0°. The mechanical angle of an entire electrical cycle is 45 degrees since the 12 stator poles and 8 rotor teeth are symmetrically arranged. Fig. 7 shows a side cross-sectional view of the magnetic field distribution when the angular position is 0°. The flux bias arising from the PM rings forms a closed homopolar vertical magnetic circuit.

C. ROTOR SUPPORT STIFFNESS AND CURRENT-FORCE COEFFICIENT SIMULATION

K_z and K_θ were calculated from the slopes of the restoring force and torque versus axial displacement ranging from 0-0.3 mm and tilt angle ranging from 0-30 mrad, respectively. K_c and K_s were calculated by a linear fit of the radial forces generated by varying the input current into the coil windings from 0 to 1 A and the rotor position in the radial direction from 0 to 0.3 mm, respectively. Figs. 8 (a) and (b) show the restoring force and torque simulation results at different rotor positions with rotor mechanical angles of 0 and 22.5 degrees. Linearization curves were drawn to calculate the passive axial and tilt stiffnesses. Fig. 8 (c) shows the attractive force simulation results at different radial displacements with rotor

mechanical angles of 0 and 22.5 degrees. Fig. 8 (d) shows the positioning force at different injection currents with rotor mechanical angles of 0 and 22.5 degrees. The linearization curves were also fitted to calculate the negative radial stiffness and current-force radial coefficient. Table 1 shows the results of fitting for the rotor support stiffness and the current-force coefficient, and the target values. The axial and tilt passive stiffnesses K_z and K_θ, the negative radial stiffness K_s, and the radial current-force coefficient K_c are slightly different at mechanical angles of 0 and 22.5 degrees due to a doubly salient BELSRM structure, which leads to a magnetic resistance variation with rotor mechanical angle. However, these parameters are almost independent of the rotor mechanical angle due to the uniform distribution of the homopolar biased flux generated by the two PM rings in the air gap. There are many benefits arising from the decoupled relationships between these parameters and the rotor mechanical angle. First, considering the independence of the negative radial stiffness K_s and the radial current-force coefficient K_c, a constant direct current (DC) can be used to generate a constant radial force during rotation, making radial positioning control much more effortless. Second, constant passive stabilization at arbitrary angles can be achieved. Moreover, both simulated values of the passive stiffness in the axial and tilt directions exceed the target values due to the triple-layer sliced homopolar magnetic field in the air gap, which can increase the amount of fringing flux compared with the previous single-layer or double-layer structures.

D. ROTATIONAL TORQUE SIMULATION

The rotational torque was simulated with different phase excitation methods depending on the rotor mechanical angle. Single-phase and dual-phase excitation methods were considered to evaluate the effect on the torque ripple and calculate the average torque during one electrical cycle. The conventional single-phase excitation method was used, as shown in Fig. 9, in which each of the U, V, and W phases was alternately energized during rotation through a total mechanical
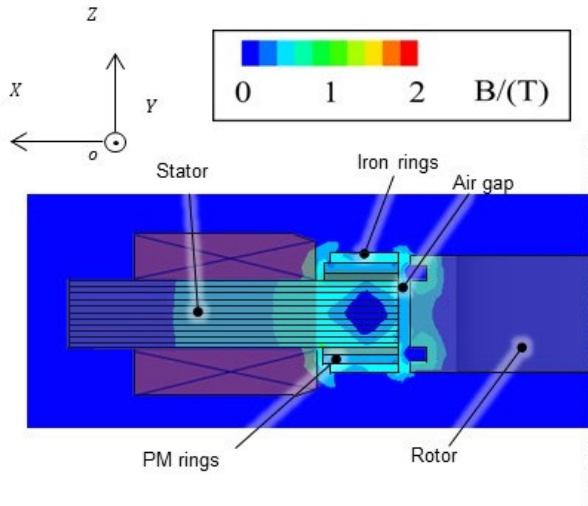
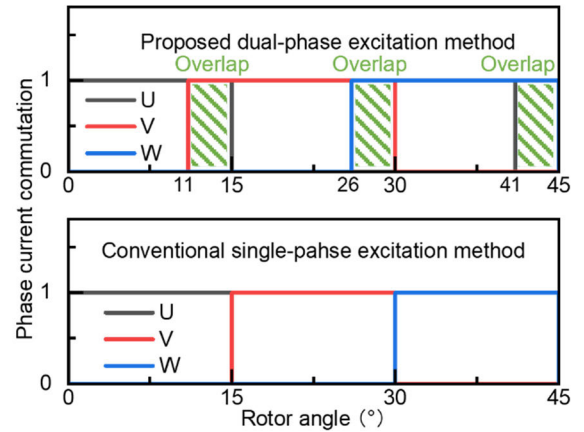**FIGURE 7.** Side cross-sectional view of the magnetic field distribution.

(a) Restoring force in the axial direction.

(b) Restoring torque in the tilt direction.

(c) Attractive force in the radial direction.

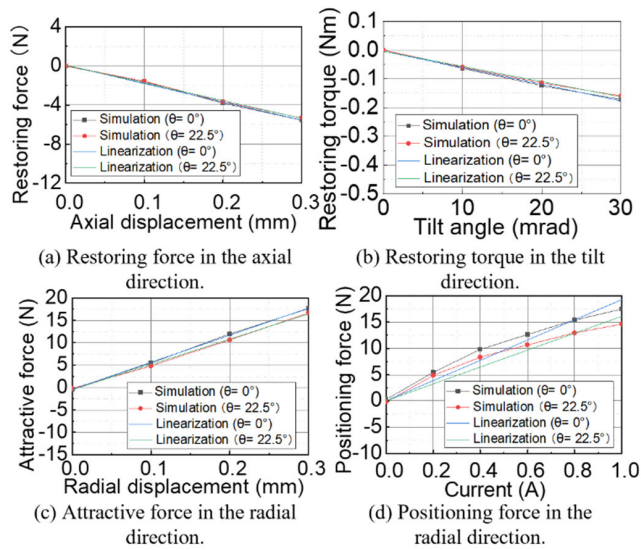(d) Positioning force in the radial direction.

FIGURE 8. Rotor support stiffness and current-force coefficient simulation results.

angle of 45°. In the dual-phase excitation method, each phase was energized during rotation through a mechanical angle of 19° for each phase. The excitation period of each phase overlaps with that of another phase, as shown in Fig. 9. The rotational torque was calculated at a constant current density of 1.8 A/mm² in a coil with a cross-sectional area of 124.8 mm².

Fig. 10 shows the rotational torque versus rotor angle with the two different phase excitation methods. There is a significant drop in rotational torque with the conventional single-phase excitation method due to the current switching between the two phases at the end of the 15° mechanical angle rotation, as shown in Fig. 10. In this position, the rotor teeth align with the energized stator pole and rotational torque cannot be produced due to the small change in magnetic
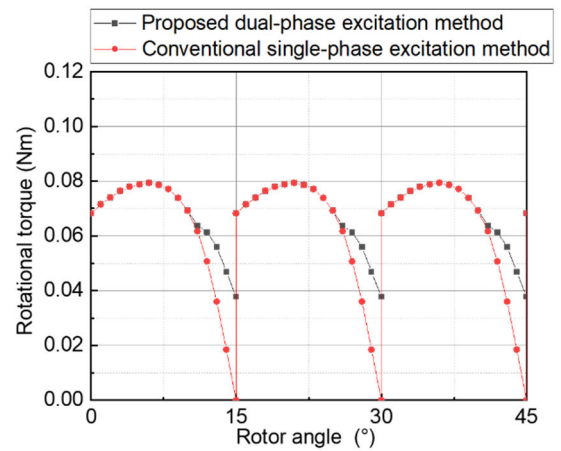

FIGURE 9. Dual-phase and single-phase excitation methods.

FIGURE 10. Rotational torque using the dual-phase and single-phase excitation methods.

resistance between the rotor teeth and the stator pole. The dual-phase excitation method was used so that the next energized winding of the stator pole is energized earlier and attracts the corresponding rotor teeth in advance, thus nullifying the absence of torque generation at 15°. This reduces torque ripple and increases the average torque. Table 1 also shows the calculation result of the average torque T_d utilizing the dual-phase excitation method, and the target value.

E. COMPARISON
The simulation results show the proposed BELSRM structure meets the specified motor torque and passive stiffness requirements. Compared with previous research [19] with a rotor with the same outer diameter and magnetic gap of the same length, the proposed BELSRM has a more straightforward and compact slice structure and combined winding construction. Besides, the proposed unique triple-layer rotor slice structure can provide more magnetic bias circuits to significantly increase the axial and tilt stiffnesses. The triple-layer rotor slice structure can reduce the effect of the rotor angle on the passive stiffness in the axial and tilt directions.

TABLE 4. Comparison between the previous and the proposed BELSM.

| Parameter		Previous	Proposed
Dimension [mm]	Rotor outer diameter	50	50
	Rotor height	15	13.4
	Stator outer diameter	114	144
	Stator thickness	44.2	18.8
	Magnetic gap	1.5	1.5
Structure	Rotor	Double-layer	Triple-layer
	Winding	Separate winding	Combined winding
BELSM Characteristics	Axial stiffness [N/mm]	3.50	18.0
	Tilt stiffness [Nm/rad]	0.87	5.9
	Average torque [Nm]	0.069	0.068
Biased flux generation		Winding current	PM rings
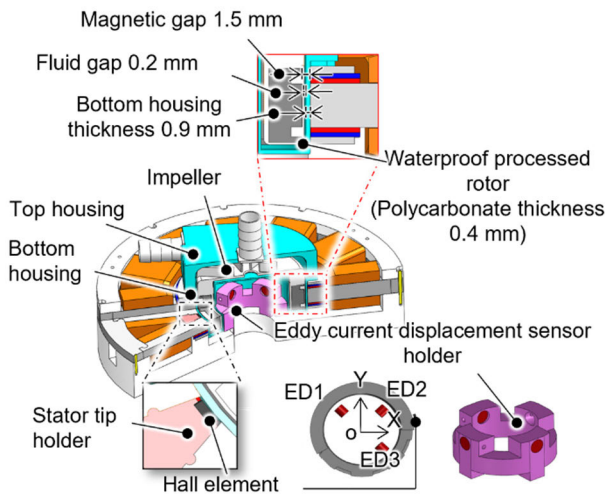
FIGURE 11. Schematic of the mechanical structure of BELSRM.

Since the magnetic flux bias is generated by the PM rings, the proposed BELSRM can minimize the power consumption and heat generation while generating the same rotational torque. A comprehensive comparison between the proposed BELSRM and previous research is summarized in Table 4.

IV. PROTOTYPE FABRICATION

A. MECHANICAL STRUCTURE

The proposed BELSRM was fabricated with the same dimensions used in the simulations. A schematic illustration showing the structure of the centrifugal pump, including the BELSRM, is shown in Fig. 11. Fig. 12 shows a photograph
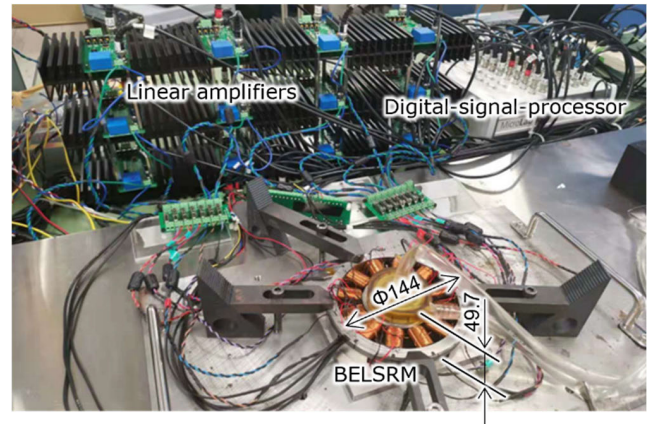
FIGURE 12. Photograph of the proposed BELSRM.

of the BELSRM with a digital-signal-processor (DSP) and linear power amplifiers. The centrifugal blood pump system consists of the BELSRM, a disposable pump head, and sensor, power, and control systems. The disposable pump head is vertically inserted into the BELSRM stator until the bottom housing touches the upper iron ring of the stator. An eddy current displacement sensor holder made of polyetherimide is placed inside the rotor to measure the radial displacement. Twelve stator tip holders made of polyetherimide are mounted between the twelve stator poles to position the stator poles around the circumference. A Hall element (HE) is affixed in the groove of the stator tip holder to detect the rotational angle and speed. The overall height of the BELSRM with the disposable pump head installed is approximately 49.7 mm.

B. DISPOSABLE PUMP HEAD

Fig. 13 shows a cross-sectional view and photograph of the disposable pump head. The disposable pump head comprises a top housing, bottom housing, and integrated impeller/rotor. The top and bottom housing, made of polyetherimide, are assembled by screws and sealed by a rubber shim with a thickness of 1 mm. The top housing is drilled to connect to the inlet and outlet which have inner diameters of 9 mm. The bottom housing is recessed in the middle from the bottom surface to provide enough space to install the eddy current displacement sensor holder for radial displacement measurements. The integrated impeller/rotor consists of an iron rotor and a polycarbonate impeller. The iron rotor is embedded in a polycarbonate mold. For waterproofing, epoxy resin is dipped into the gap between the iron rotor and the polycarbonate mold. After evacuation and standing for 36 hours, the whole part is machined into the shape of an impeller. The diameter and height of the integrated impeller/rotor are 50.8 mm and 27.9 mm, respectively. The flat impeller has six straight 5.5 mm high vanes and a $\Phi6$ mm washout hole for secondary flow to avoid blood stagnation. The mass of the integrated impeller/rotor is 0.088 kg. When the impeller/rotor is suspended in the geometric center, the upper, lower, and lateral
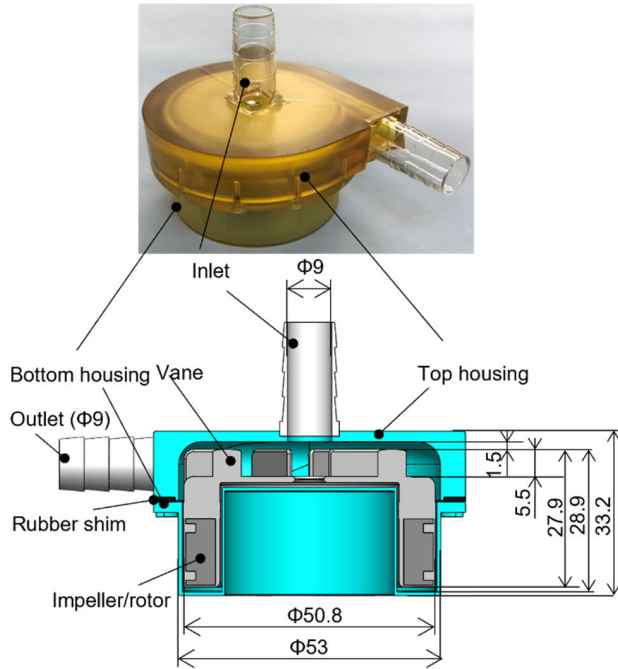
FIGURE 13. Photograph and cross-section view of the disposable pump head.

FIGURE 14. Block diagram of the rotor angle signal processing.

FIGURE 15. (a) Raw HE signal and (b) filtered HE signal at different rotational speeds of 1600 rpm and 2400 rpm.

fluid gaps between the rotor and the housing are 1.5 mm, 1 mm, and 0.2 mm, respectively.

C. SENSOR SYSTEM

Fig. 11 shows the overall sensor configuration, including the three eddy current displacement sensors and one Hall element for measuring the radial displacement and the angle of rotation. The three displacement sensors (PU-05A, AEC Corp, Japan) are mounted inside the rotor at ± 45 and $135°$ with respect to the X-axis. The measurement range of the displacement sensors is 0-2 mm, and the resolution is $0.3\ \mu$m. The rotor displacements in the X- and Y-directions are calculated by the difference values from the three eddy current displacement sensors using equations (1) and (2). The temperature drift and common-mode noise of the displacement sensors can be suppressed.

$$x = \frac{ED_2 - ED_1}{\sqrt{2}} \tag{1}$$

$$y = \frac{ED_2 - ED_3}{\sqrt{2}} \tag{2}$$

where ED_1, ED_2, and ED_3 are the output signals of the three eddy current displacement sensors.

Precise rotor angle measurements are significant for phase current commutation to improve the rotational torque in closed-loop control. Due to the space constraints of the proposed sliced BELSRM, the Hall element for measuring the rotor angle is mounted midway between the two stator poles. The flux bias generated by the PM rings passes through the HE and the impeller/rotor. Due to the salient rotor structure, the output voltage of the HE varies at a frequency of eight
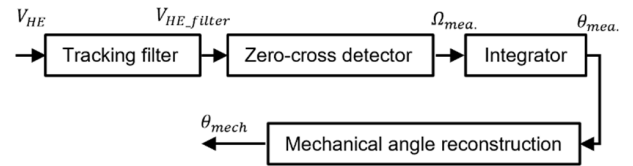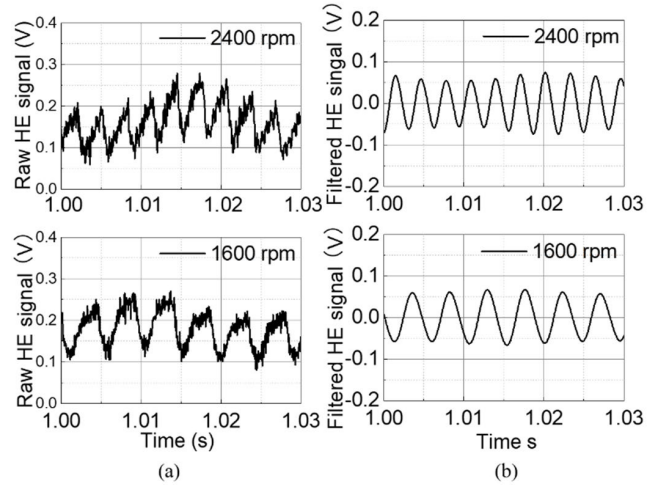
times the rotational speed when the rotor is rotating. However, flux arising from motor current commutation has the same frequency of eight times the rotational speed, which also crosses the HE due to its mounting position close to the stator poles, leading to distortion of the output voltage. As the rotational speed increases, the motor current also increases, causing more severe output voltage distortion and rotor angle measurement errors. A low-sensitivity Hall element (HG-372A, AKM Corp., Japan) was used and mounted between the X_{pw} and X_{pv} phase stator poles to reduce the effect of the motor flux on the rotor angle measurement. A block diagram of the rotor angle signal processing is shown in Fig. 14. A tracking filter was used to suppress the noise in the output voltage signal from the Hall element (V_{HE}), and the center frequency was set as the reference rotational speed. A zero-cross detector was utilized to calculate the rotational speed. The rotor mechanical angle was obtained by integrating the rotational speed from the zero-cross point detected by the zero-cross detector. The rotor mechanical angle signal was reconstructed based on the reference rotational speed and the moment when the measured mechanical angle $\theta_{mea.}$ was 0.

The filtered HE signals, as shown in Fig. 15 (b), are obtained from the raw HE signal, as shown in Fig. 15 (a), at different rotational speeds of 1600 rpm and 2400 rpm. The amplitude of the filtered HE signal at 2400 rpm has an apparent variation, which is affected by the motor flux. The rotor angle signal processing mentioned above reconstructs
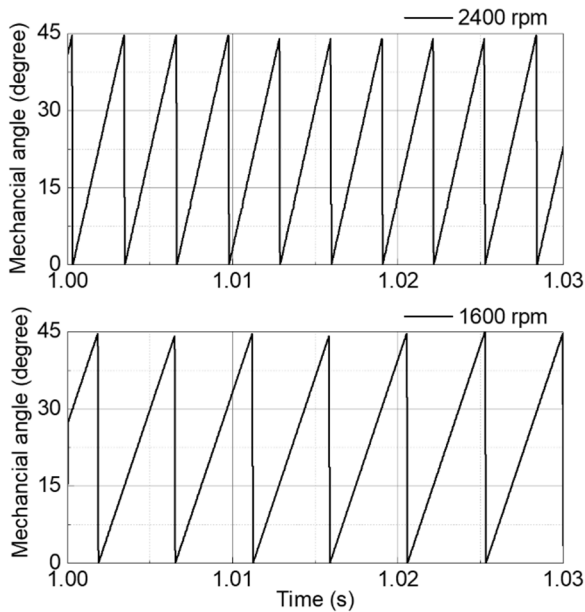
FIGURE 16. Mechanical angle calculation at different rotational speeds of 1600 rpm and 2400 rpm utilizing rotor signal processing.

FIGURE 17. Measured bode diagram of the current closed-loop feedback system I_{out}/I_{ref}.

the rotor angle signal further to reduce the effect of the filtered HE signal distortion. Fig. 16 shows the calculation of the mechanical angle utilizing the rotor signal processing. The calculated mechanical angle error increases with rotational speed. The maximum mechanical angle error is approximately 1.1 degrees at a speed of 2400 rpm, which is acceptable.

D. POWER SYSTEM

Twelve linear power amplifiers (PA04, Apex Microtechnology, Inc., USA) were used to deliver electric power to the twelve concentrated windings. The diameter of the coil wire is 0.55 mm and the average resistance and inductance of the twelve concentrated coils are 2.22 Ω and 27.7 mH, respectively. The maximum supply voltage of the linear power amplifiers is ±60 V due to temperature limitations. Twelve Hall-effect current sensors (LA25-NP, LEM Corp.) were used to independently measure the current in each combined winding. The measured current value was utilized in the PI controller to realize closed-loop current regulation. The proportional and integral gain values are set at 160 V/A and 800 V/A·s, respectively. The bode diagram of the current closed-loop feedback system was measured during magnetic levitation, as shown in Fig. 17. The amplitude of the reference current is 0.05 A and the bandwidth of the current closed-loop feedback system I_{out}/I_{ref} is about 780 Hz.

E. CONTROL SYSTEM

Fig. 18 shows the suspension and rotation control systems of the BELSRM. A DSP (MicroLabBox, dSPACE, GmbH.) delivers current reference commands to the twelve coil windings through twelve linear power amplifiers. The suspension
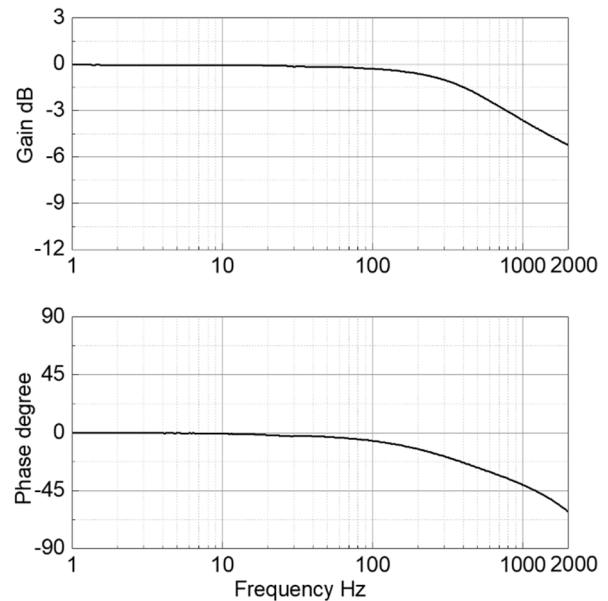
and rotation control systems are implemented utilizing the DSP system with a sampling frequency of 20 kHz. Both the analog input and analog output are 16-bit channels. Both input and output voltage ranges are ±10 V.

In the suspension control system, a proportional-integral-derivative (PID) controller is implemented for radial displacement feedback and a first-order low pass filter (LPF) with a cut-off frequency f_{l1} is added to the derivative part in the PID controller to limit the high-frequency gain. A second-order LPF with damping ratio ζ and cut-off frequency f_{l2} is added to the output of the displacement sensor to suppress high-frequency noise. The control parameters are tuned experimentally, as shown in Table 5. Bode diagrams of the displacement closed-loop feedback system in the X- and Y-directions were measured. The amplitude of the reference displacement is 30 μm and the bandwidth of the displacement closed-loop feedback system X_{out}/X_{ref} is about 61 Hz, as shown in Fig. 19. A zero-power controller (G_{zero}) is used only to determine the magnetic center in levitation, but not used in the rotation experiment due to the combined windings. The determined magnetic center is defined by the reference radial position that minimizes the levitation consumption. This controller consists of an integral operator and has a gain of 0.001 m/A·s.

Twelve linear power amplifiers divided into four groups X_n, X_p, Y_n, Y_p are energized to inject the reference current from the PID controller into the twelve coils to generate radial forces in the X- and Y-directions. The synchronous disturbance elimination method [22] compensates for unbalanced vibrations by extracting the rotation frequency vibration amplitude from the measured displacement signal.

In the rotation control system, closed-loop feedback control is used to improve the rotational torque by rotor angle
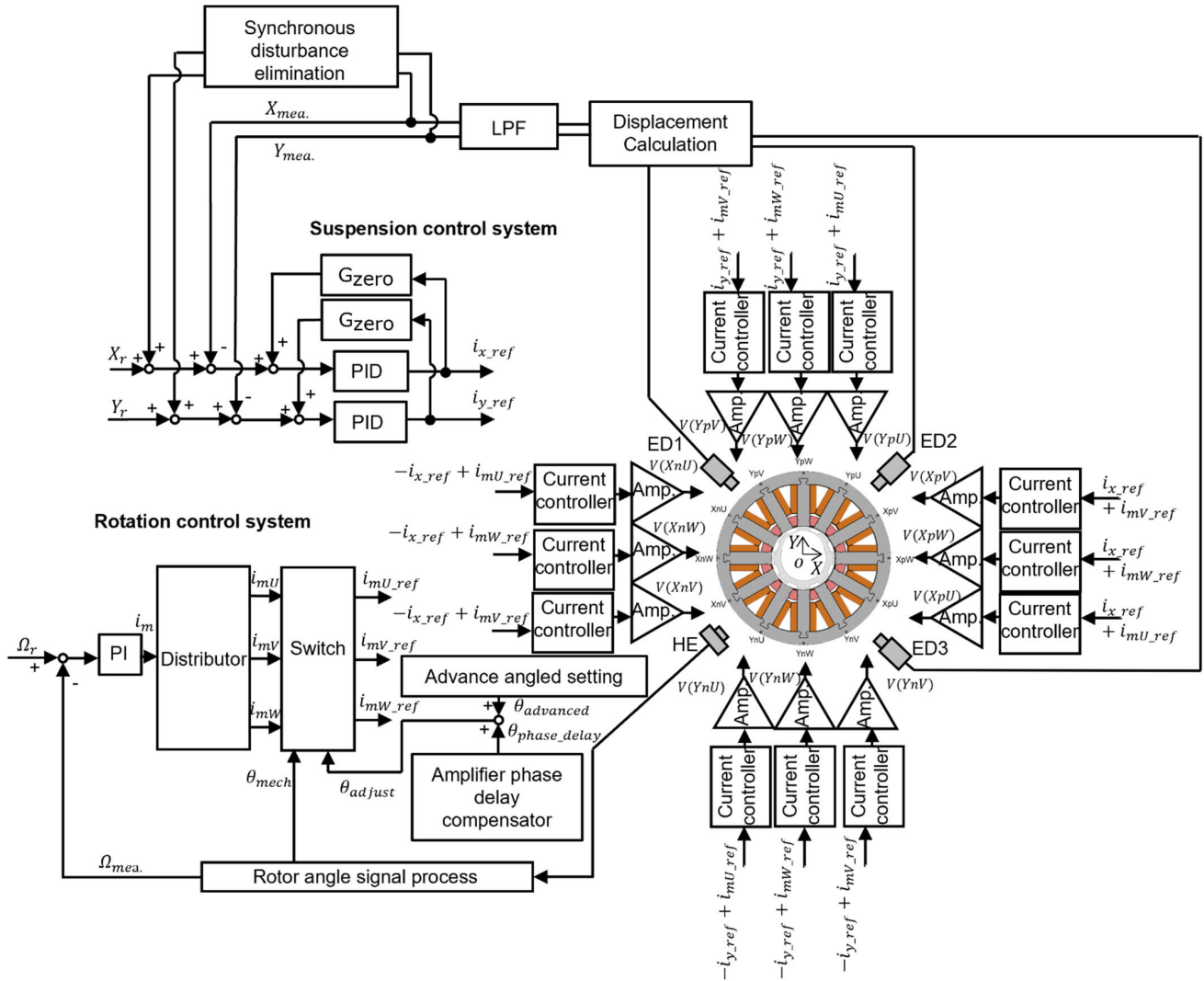
FIGURE 18. Block diagram for suspension and rotation control system.

measurement and current commutation. A PI controller, as shown in Table 5, is used to calculate the amplitude of the reference current i_m. Simulation and experiment were done to determine the current commutation based on the rotor angle measurements at each rotational speed to improve the rotational torque. The mechanical angle is calculated from the raw Hall sensor signal through the rotor angle signal processing method mentioned above. Three phases U, V, and W are excited at different mechanical angles to generate reference rectangular wave currents i_{mU_ref}, i_{mV_ref}, i_{mW_ref}. The dual-phase excitation method is used, and the current excitation period for each phase coil is set to $22.5°$, which was determined by simulation to generate the maximum rotational torque. An amplifier phase delay compensator θ_{phase_delay} and an advanced angle setting $\theta_{advanced}$ are added to improve the rotational torque, as shown in Fig. 18. The amplifier phase delay compensator θ_{phase_delay} is used to compensate for the current-loop feedback phase delay I_{out}/I_{ref}, as shown

in Fig. 17. A cubic function is used to fit the measured phase bode plot to calculate θ_{phase_delay} at each rotational speed. The advanced angle setting $\theta_{advanced}$ is used to reduce the effect of the current response delay depending on the rotational speed, as shown in Table 6. The advanced angle setting $\theta_{advanced}$ is experimentally tuned so that the current amplitude is the smallest at each rotational speed. The adjustment angle θ_{adjust}, which is the sum of θ_{phase_delay} and $\theta_{advanced}$, is subtracted from the energized mechanical angle of each phase. Table 7 shows the phase commutation of the mechanical angle of each phase.

V. EXPERIMENTAL RESULTS
A. EXPERIMENTAL SETUP
As shown in Fig. 20, the mock circulatory loop consists of the proposed centrifugal blood pump, two pressure gauges (GP-M001, KEYENCE; KL-76, Naganokeiki) placed at the inlet and outlet of the pump head, an ultrasonic flowmeter (TS410,

TABLE 5. Displacement and speed feedback control parameters.

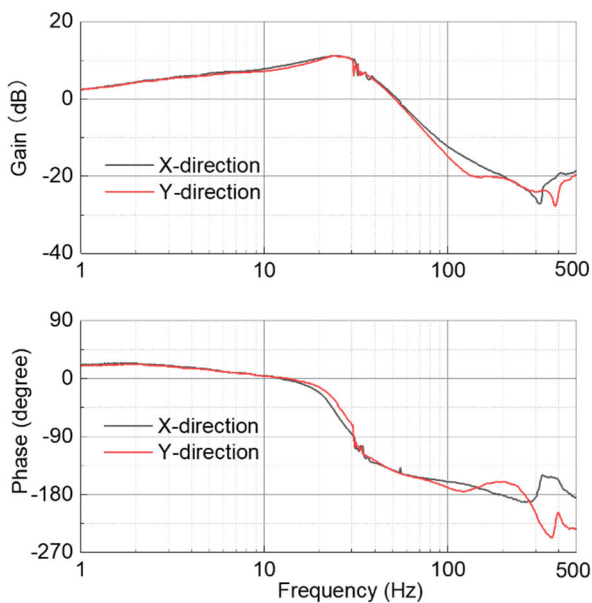| Parameters	Suspension control system	Rotation control system
Proportional gain K_p	4300 A/m	0.005 A/rpm
Integral gain K_i	20000 A/m·s	0.001 A/rpm·s
Derivative gain K_d	7A·s /m	-
Cut-off frequency of the first-order LPF f_{l1}	500 Hz	-
Cut-off frequency of the second-order LPF f_{l2}	140 Hz	
Damping ratio of the second-order LPF ζ	1	

TABLE 6. Advanced angle setting depending on the rotational speed.

Rotational speed (rpm)	Advanced angle degree (degree)
1600	-2.5
1800	-3.0
2000	-3.8
2200	-5.5
2400	-7.5

TABLE 7. Phase commutation of the mechanical angle for *U*, *V*, and *W* phase.

Motor phase		*U* phase	*V* phase	*W* phase
Energized mechanical angle (degree)	On	$-7.5-\theta_{adjust}$	$7.5-\theta_{adjust}$	$22.5-\theta_{adjust}$
	Off	$15-\theta_{adjust}$	$30-\theta_{adjust}$	$45-\theta_{adjust}$

FIGURE 19. Measured bode diagrams of the displacement closed-loop feedback system X_{out}/X_{ref}.
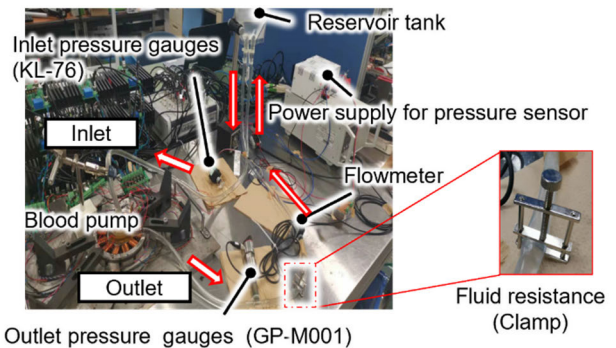
FIGURE 20. Mock circulatory loop for pump performance evaluation.

Transonic Systems, Inc.), a reservoir tank, and a clamp to regulate the fluid resistance. The mock circulatory loop was filled with 40 wt% aqueous glycerol solution to simulate the approximate blood viscosity conditions in a natural working environment. The viscosity of the 40 wt% glycerol aqueous solution is 3.63 mPa·s at 20°C(room temperature), which is within the range of blood viscosity (3-4 mPa·s) at 37°C (body temperature).

B. MAGNETIC LEVITATION
A magnetic levitation experiment was conducted with the outlet fully clamped, and the pump housing filled with a 40 wt% aqueous glycerol solution. In the magnetic levitation start-up experiment, the impeller/rotor can be stably levitated,

and the positioning accuracy was evaluated at a speed of 0 rpm, as shown in Fig. 21. The maximum amplitudes of the displacements in the X- and Y-directions were 14.5 μm and 10.5 μm, respectively. Fig. 22 (a) and (b) show the current and voltage in the magnetic levitation experiment.

C. ROTATIONAL ACCURACY
Stable rotation from 0 rpm to 2300 rpm in a 40wt% aqueous glycerol solution was achieved. Fig. 23 shows the rotation accuracy of the impeller/rotor versus rotational speed at the maximum flow rate in the radial X- and Y- directions from 1600 rpm to 2300 rpm. The maximum amplitudes of the displacements in the X- and Y-directions are smaller than 100 μm, and there is no risk of physical contact between the impeller/rotor and the housing wall. Fig. 24 shows the rotation trajectory of the impeller at a speed of 2300 rpm with different flow rates. The maximum vibrational amplitude of
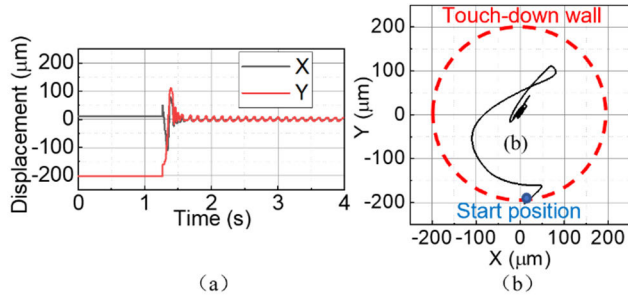
FIGURE 21. Magnetic levitation experiment without rotation.
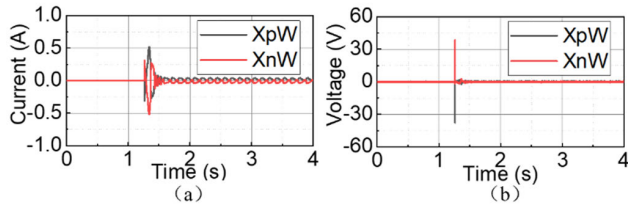(a) Displacement. (b) Trajectory.

FIGURE 22. Magnetic levitation experiment without rotation. (a) Current.
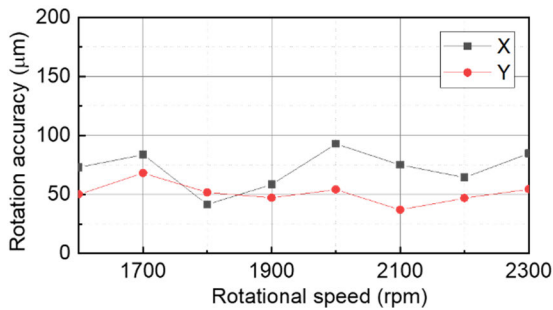(b) Voltage.

FIGURE 23. Measured rotation accuracy of the impeller/rotor versus
rotational speed at each maximum flow rate in the X- and Y- directions.

the impeller/rotor trajectories is less than 100 μm at the maximum flow rate. Since the fluid gap is 200 μm, the vibrational amplitude does not exceed 50% when the rotor rotates at high flow rates and rotational speeds.

D. PUMP HYDRAULIC PERFORMANCE
The *H-Q* curve, power consumption and pump efficiency were measured in the mock circulatory loop. The *H-Q* curve was measured at designated rotational speeds by changing the fluid resistance with the clamp. The power consumption $\bar{P}$ of the proposed BELSRM was calculated using the following equation (3), which is the average of the product of twelve coil currents and voltages within multiple rotation cycles, excluding the power consumption of the linear power amplifiers and the sensor system.

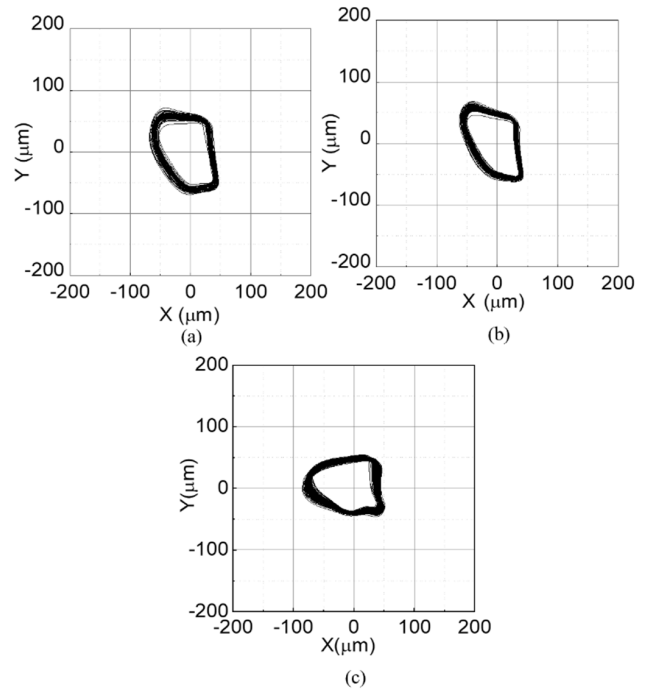$$\bar{P} = \frac{\sum_{c=1}^{12} V_c(N) I_c(N)}{N} \quad (3)$$

FIGURE 24. Measured rotation trajectory of the impeller/rotor at a speed of 2300 rpm with different flow rates: (a) 0 L/min. (b) 1.99 L/min.
(c) 4.59 L/ min.

where $V_c(N)$ and $I_c(N)$ represent the transient twelve coil currents and voltages in the discretized time domain measured by the current and voltage sensors, respectively. N is the number of sampling points in the operational period. The pump efficiency η was evaluated from the average power consumption in the *H-Q* curve according to equation (4):

$$\eta = \frac{HQ}{\bar{P}} \quad (4)$$

where H is the head pressure of the centrifugal blood pump calculated by the pressure difference between the inlet and the outlet, and Q is the flow rate measured by the flow rate sensor.

Fig. 25 illustrates the hydraulic performance of the CBPs utilizing the proposed BELSRM from 1600 rpm to 2400 rpm, which involves (a) the *H-Q* curve; (b) the power consumption; (c) the pump efficiency. The maximum head pressure and maximum flow rate achieved were 214.5 mmHg and 4.59 L/min at rotational speeds of 2400 rpm and 2300 rpm, respectively, as shown in Fig. 25 (a). The power consumption is the sum of the power used for magnetic levitation and rotation, as shown in Fig. 25 (b), which increases with rotational speed and flow rate. The pump efficiency rises gradually and reaches a maximum value, as seen in Fig. 25 (c). The maximum pump efficiency in our experiment was 5.3% at a speed of 2300 rpm with a flow rate of 4.48 L/min.

VI. DISCUSSION
The CBP with a BELSRM provided a maximum head pressure of 214.5 mmHg and a maximum flow rate of 4.59 L/min
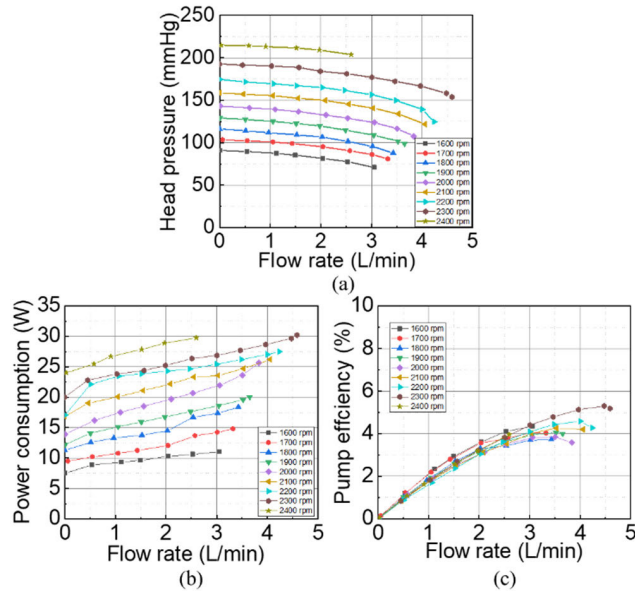
FIGURE 25. Hydraulic performance of the CBPs utilizing the proposed BELSRM. (a) H-Q curve. (b) Power consumption. (c) Pump efficiency.
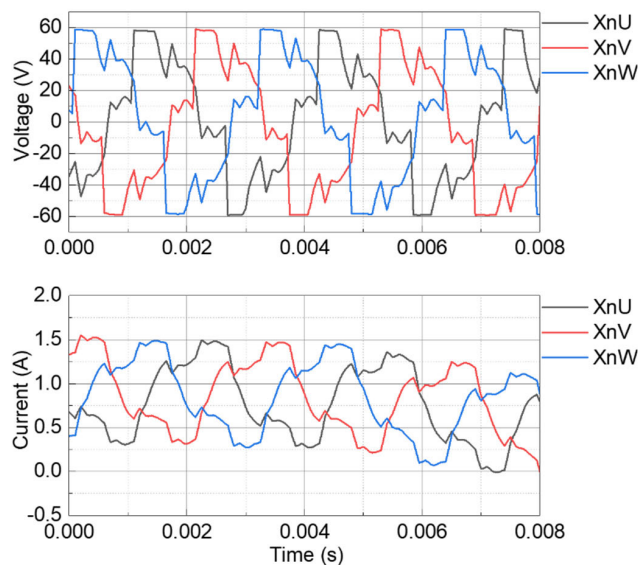

FIGURE 26. Current and the input voltage of the coils at a maximum speed of 2400 rpm with a maximum flow rate of 2.60 L/min.

with stable levitation. However, the CBP did not fully achieve the hydraulic performance requirements for an ECMO due to the rotational speed limit. The impeller/rotor cannot stably rotate at high speeds with high flow rates due to insufficient torque and bearing stability. The main reason is the relatively low current-loop bandwidth of 780 Hz which is a result of the insufficient output voltage ±60 V from the linear power amplifiers due to temperature limitations. Fig. 26 shows the current and the input voltage of the coils at a maximum speed of 2400 rpm with a maximum flow rate of 2.60 L/min. The voltage has noticeable saturation due to
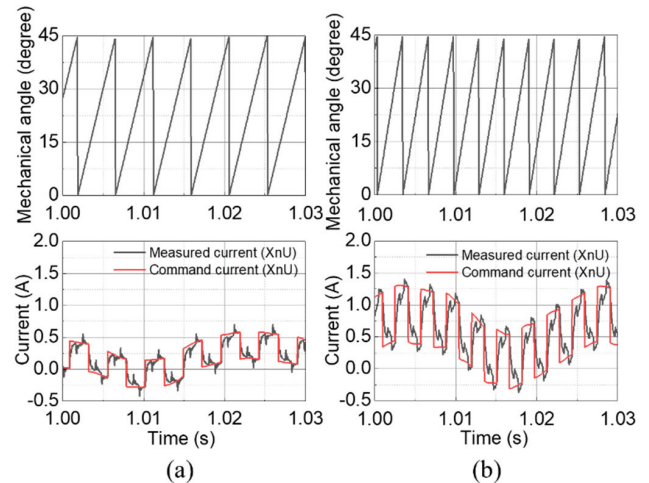

FIGURE 27. Relationship among the calculated mechanical rotor angle, command current and measured current. (a) 1600 rpm. (b) 2400 rpm.

the insufficient voltage supplied to the linear power amplifiers. Figs. 27 (a) and (b) show the relationships between the calculated mechanical angle, the command current, and the measured current at speeds of 1600 rpm and 2400 rpm without flow, respectively. The lower current-loop bandwidth prevents the motor and suspension current amplitudes from following the command current precisely enough at high rotational speeds, leading to insufficient torque and levitation stability.

In future, power amplifiers with higher saturation voltages must be used to produce sufficient output voltage, achieving high current-loop bandwidth and avoiding voltage saturation, which can also reduce power consumption and increase the pump efficiency.

VII. CONCLUSION

A low-cost and compact disposable CBP utilizing a homopolar 12/8 switched reluctance type bearingless slice motor was proposed. This removes the need for expensive PMs in the rotor. Two PM rings symmetrically arranged on the stator pole tip form a triple-layer magnetic field with an iron rotor with top and bottom flanges, providing a high torque density for rotation, high passive stiffness for portability and easy positioning control for radial levitation. To evaluate the performance of the proposed pump, a prototype BELSRM with a disposable pump head was fabricated and tested. The positioning and rotation performance of the BELSRM were evaluated in a 40 wt% aqueous glycerol solution. The impeller/rotor could be levitated and rotated at a speed of 2300 rpm with a maximum flow rate of 4.59 L/min with a positioning error of less than 100 μm. Evaluation of the hydraulic performance of the pump was also carried out. The pump demonstrated a maximum flow rate of 4.59 L/min and a maximum head pressure of 214.4 mmHg at speeds of 2300 rpm and 2400 rpm, respectively. The maximum pump efficiency is 5.3%.

REFERENCES

[1] C. Schmid, C. Etz, H. Welp, M. Rothenburger, H. Reinecke, M. Schafers, C. Schmidt, and H. Scheld, "Clinical situations demanding weaning from long-term ventricular assist devices," *Eur. J. Cardio-Thoracic Surg.*, vol. 26, no. 4, pp. 730–735, Oct. 2014.

[2] M. Thalmann, H. Schima, G. Wieselthaler, and E. Wolner, "Physiology of continuous blood flow in recipients of rotary cardiac assist devices," *J. Heart Lung Transplantation*, vol. 24, no. 3, pp. 237–245, Mar. 2005.

[3] J. Sinard and R. Bartlett, "Review articles: Extracorporeal membrane oxygenation (ECMO): Prolonged bedside cardiopulmonary bypass," *Perfusion*, vol. 5, no. 4, pp. 239–249, Oct. 1990.

[4] A. R. Kherani, S. Maybaum, and M. C. Oz, "Ventricular assist devices as a bridge to transplant or recovery," *Cardiology*, vol. 101, nos. 1–3, pp. 93–103, 2004.

[5] K. D. Aaronson, M. J. Eppinger, D. B. Dyke, S. Wright, and F. D. Pagani, "Left ventricular assist device therapy improves utilization of donor hearts," *J. Amer. College Cardiol.*, vol. 39, no. 8, pp. 1247–1254, Apr. 2002.

[6] E. A. Ziemba and R. John, "Mechanical circulatory support for bridge to decision: Which device and when to decide," *J. Cardiac Surgery*, vol. 25, no. 4, pp. 425–433, Apr. 2010.

[7] G. P. Noon, D. Morley, S. Irwin, and R. Benkowski, "Development and clinical application of the MicroMed DeBakey VAD," *Current Opinion Cardiol.*, vol. 15, no. 3, pp. 166–171, May 2000.

[8] O. H. Frazier, T. J. Myers, I. D. Gregoric, T. Khan, R. Delgado, M. Croitoru, K. Miller, R. Jarvik, and S. Westaby, "Initial clinical experience with the Jarvik 2000 implantable axial-flow left ventricular assist system," *Circulation*, vol. 105, no. 24, pp. 2855–2860, Jun. 2002.

[9] B. P. Griffith, R. L. Kormos, H. S. Borovetz, K. Litwak, J. F. Antaki, V. L. Poirier, and K. C. Butler, "HeartMate II left ventricular assist system: From concept to first clinical use," *Ann. Thoracic Surg.*, vol. 71, no. 3, pp. 116–120, 2001.

[10] J. Asama, T. Shinshi, H. Hoshi, S. Takatani, and A. Shimokohbe, "A compact highly efficient and low hemolytic centrifugal blood pump with a magnetically levitated impeller," *Artif. Organs*, vol. 30, no. 3, pp. 160–167, Mar. 2006.

[11] T. Someya, M. Kobayashi, S. Waguri, T. Ushiyama, E. Nagaoka, W. Hijikata, T. Shinshi, H. Arai, and S. Takatani, "Development of a disposable maglev centrifugal blood pump intended for one-month support in bridge-to-bridge applications: In vitro and initial in vivo evaluation," *Artif. Organs*, vol. 33, no. 9, pp. 704–713, Sep. 2009.

[12] D. Steinert, T. Nussbaumer, and J. W. Kolar, "Slotless bearingless disk drive for high-speed and high-purity applications," *IEEE Trans. Ind. Electron.*, vol. 61, no. 11, pp. 5974–5986, Nov. 2014.

[13] J. Asama, D. Kanehara, T. Oiwa, and A. Chiba, "Performance investigation of a centrifugal pump with a consequent-pole bearingless motor," in *Proc. IEEE Energy Convers. Congr. Expo. (ECCE)*, Raleigh, NC, USA, Sep. 2012, pp. 3663–3669.

[14] W. Hijikata, T. Shinshi, J. Asama, L. Li, H. Hoshi, S. Takatani, and A. Shimokohbe, "A magnetically levitated centrifugal blood pump with a simple-structured disposable pump head," *Artif. Organs*, vol. 32, no. 7, pp. 531–540, Jul. 2010.

[15] W. Hijikata, T. Shinshi, A. Shimokohbe, H. Sobajima, and S. Takatani, "Disposable Maglev centrifugal blood pump utilizing a cone-shaped impeller," *Artif. Organs*, vol. 34, no. 8, pp. 669–677, 2010.

[16] W. Hijikata, T. Mamiya, T. Shinshi, and S. Takatani, "A cost-effective extracorporeal magnetically-levitated centrifugal blood pump employing a disposable magnet-free impeller," *Proc. Inst. Mech. Eng., H, J. Eng. Med.*, vol. 225, no. 12, pp. 1149–1157, Dec. 2011.

[17] T. Holenstein, M. Schuck, and J. W. Kolar, "A wide air gap flux switching bearingless motor with odd and even pole pair numbers," *IEEE Open J. Ind. Appl.*, vol. 1, pp. 52–62, 2020.

[18] T. Holenstein, M. Schuck, and J. W. Kolar, "Performance benchmarking of a novel magnet-free bearingless synchronous reluctance slice motor," *IEEE Open J. Ind. Electron. Soc.*, vol. 1, pp. 184–193, 2020.

[19] J. Rao, W. Hijikata, and T. Shinshi, "A bearingless motor utilizing a permanent magnet free structure for disposable centrifugal blood pumps," *J. Adv. Mech. Des., Syst., Manuf.*, vol. 9, no. 3, 2015, Art. no. JAMDSM0046.

[20] K. Raggl, T. Nussbaumer, and J. W. Kolar, "A comparison of separated and combined winding concepts for bearingless centrifugal pumps," *J. Power Electron.*, vol. 9, no. 2, pp. 243–258, 2009.

[21] J. Asama, T. Fukao, A. Chiba, A. Rahman, and T. Oiwa, "A design consideration of a novel bearingless disk motor for artificial hearts," in *Proc. IEEE Energy Convers. Congr. Expo.*, San Jose, CA, USA, Sep. 2009, pp. 1693–1699.

[22] A. Chiba, T. Fukao, and O. Ichikawa, *Magnetic Bearings and Bearingless Drive*. Amsterdam, The Netherlands: Elsevier, 2005, pp. 75–78.

REN YANG was born in Huaihua, Hunan, China, in 1994. He received the B.S. degree in mechanical engineering from the Dalian University of Technology, China, in 2017, and the M.S. degree in mechanical engineering from the Tokyo Institute of Technology, Japan, in 2019, where he is currently pursuing the Ph.D. degree in mechanical engineering. His research interests include magnetic bearing and bearingless motors.

ZEQIANG HE was born in Hangzhou, Zhejiang, China, in 1997. He received the B.S. degree in electrical engineering from Zhejiang University, China, in 2020, and the M.S. degree in mechanical engineering from the Tokyo Institute of Technology, Japan, in 2022, where he is currently pursuing the Ph.D. degree in mechanical engineering. His research interests include the development of the bearingless motor and its application in the blood pump.

NAOHIRO SUGITA received the B.S., M.S., and Ph.D. degrees in mechanical engineering from Keio University, Yokohama, Japan, in 2012, 2014, and 2017, respectively. From 2017 to 2019, he was a Researcher with the Products Development Center, IHI Corporation, Yokohama. Since 2019, he has been an Assistant Professor with the Laboratory for Future Interdisciplinary Research of Science and Technology, Tokyo Institute of Technology. His research interests include mechanical and acoustic resonances, nonlinear vibration, ultrasound cavitation, bubble oscillations in an ultrasound field, and medical ultrasound applications.

TADAHIKO SHINSHI (Member, IEEE) received the B.E., M.E., and Dr.Eng. degrees from the Tokyo Institute of Technology, Japan, in 1990, 1992, and 2000, respectively. From 1992 to 1995, he was with the Mechanical Engineering Research Laboratory, Hitachi Ltd. In 1995, he joined the Precision and Intelligence Laboratory (P&I Lab), Tokyo Tech, as a Research Associate and became an Associate Professor and a Professor, in 2000 and 2010, respectively. He is currently a Professor with the Institute of Innovation Research (IIR), Tokyo Tech. His current research interests include micro-mechatronics and precision motion control.

• • •